nature chemistry

Article

https://doi.org/10.1038/s41557-023-01154-9

Connecting the geometric and electronic structures of the nitrogenase iron–molybdenum cofactor through site-selective ^{57}Fe labelling

Received: 15 January 2022

Accepted: 26 January 2023

Published online: 13 March 2023

Check for updates

Edward D. Badding [1], Suppachai Srisantitham [1], Dmitriy A. Lukoyanov [2], Brian M. Hoffman [2] & Daniel L. M. Suess [1]

Understanding the chemical bonding in the catalytic cofactor of the Mo nitrogenase (FeMo-co) is foundational for building a mechanistic picture of biological nitrogen fixation. A persistent obstacle towards this goal has been that the ^{57}Fe-based spectroscopic data—although rich with information—combines responses from all seven Fe sites, and it has therefore not been possible to map individual spectroscopic responses to specific sites in the three-dimensional structure. Here we have addressed this challenge by incorporating ^{57}Fe into a single site of FeMo-co. Spectroscopic analysis of the resting state informed on the local electronic structure of the terminal Fe1 site, including its oxidation state and spin orientation, and, in turn, on the spin-coupling scheme for the entire cluster. The oxidized resting state and the first intermediate in nitrogen fixation were also characterized, and comparisons with the resting state provided molecular-level insights into the redox chemistry of FeMo-co.

Nitrogenases catalyse the reduction of N_2 to NH_3 (Fig. 1a) and, along with the Haber–Bosch process, are responsible for producing the vast majority of the fixed nitrogen that supports life on Earth[1–3]. Although the multi-electron, multi-proton generation of NH_3 from N_2 is thermodynamically feasible under ambient conditions, it is kinetically very challenging because the first step, cleavage of the N≡N triple bond, is so unfavourable. As such, the mechanism of biological N_2 fixation, particularly the chemistry that occurs at the catalytic cofactor of the Mo nitrogenase isozyme (FeMo-co), has been intensively studied for decades[3–8]. Foundational to these investigations is an understanding of FeMo-co's electronic structure: the distribution and coupling of the valence electrons in the resting state and how the electronic structure changes throughout the catalytic cycle. However, the sheer number of open-shell metal ions in FeMo-co (seven structurally unique Fe sites and one Mo centre[9]) pushes the limits of computational analysis[10–16] and, as described below, presents a number of challenges in its experimental characterization.

Whereas the Mo centre in FeMo-co can be selectively probed using Mo-specific spectroscopic techniques[17–23], the study of the individual Fe centres is more difficult. In particular, the wealth of information contained in ^{57}Fe Mössbauer and electron–nuclear double resonance (ENDOR) spectra—including the Fe oxidation states, the covalency of Fe–S/C and Fe–Fe/Mo interactions, the local spin states and the orientations of the local spins with respect to the total spin—has been challenging to extract because the ^{57}Fe spectroscopic data cannot be mapped onto the geometric structure (Fig. 1b). Even for the most well-characterized state, the resting state (E_0, with FeMo-co in the M^N state), it has not been possible to experimentally correlate the crystallographically observed Fe sites (Fe1–Fe7; Fig. 1b,c)[9] with the spectroscopically observed ^{57}Fe sites (A^1–A^4, B^1 and B^2, where the

[1]Department of Chemistry, Massachusetts Institute of Technology, Cambridge, MA, USA. [2]Department of Chemistry, Northwestern University, Evanston, IL, USA. e-mail: suess@mit.edu

https://doi.org/10.1038/s41557-023-01154-9

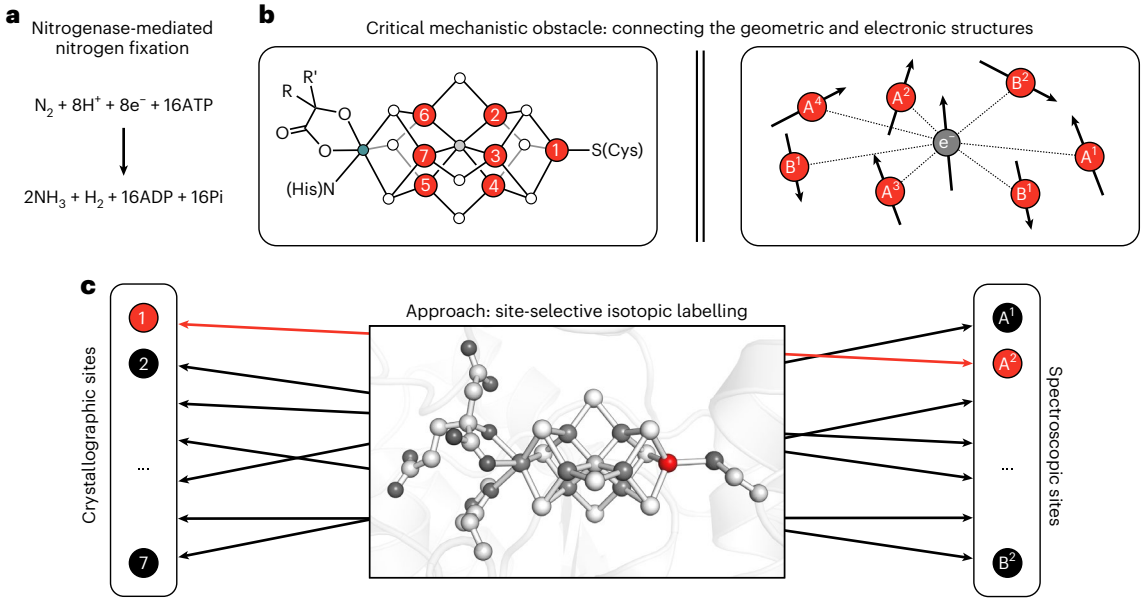

Fig. 1 | Employing site-selective isotopic labelling to understand the mechanism of biological nitrogen fixation. a, Overall reaction for the nitrogenase-mediated reduction of N_2 to NH_3. **b**, A major challenge in mechanistic studies of nitrogenases is the inability to correlate the spectroscopic data with the geometric structure. The numbers in red circles correspond to the crystallographically defined Fe sites (Fe1–Fe7). The teal, white and grey circles represent Mo, S and C atoms, respectively. R, $-CH_2CO_2^-$; R′, $-(CH_2)_2CO_2^-$. **c**, Site-selective labelling as a strategy to connect the geometric and electronic structures of FeMo-co. PDB accession code: 3U7Q (ref. [9]).

A and B sites have negative and positive isotropic hyperfine coupling constant (a_{iso}), respectively, and the B^1 site represents two equivalent Fe centres; Fig. 1b,c)[20,24–26]. For ^{57}Fe Mössbauer spectroscopy in particular, these challenges are compounded by poor resolution of the complex set of overlapping signals arising from the seven Fe sites; indeed, at zero-field, the Mössbauer spectrum of the M^N state appears as a single, broad quadrupole doublet at temperatures above 20 K (refs. [25,27]).

Building on previous ENDOR and Mössbauer studies, Yoo and co-workers undertook what still remains the most comprehensive Mössbauer spectroscopic analysis of FeMo-co (ref. [25]); although this work yielded a working set of Mössbauer parameters that have been widely employed in computational analysis, the authors acknowledge both the difficulties in simulating the Mössbauer data due to the poor resolution and the limitations of their interpretation owing to the inability to assign the spectroscopic features to specific sites in the structure. More broadly, few experimental methods allow for the mapping of the electronic structure of FeMo-co onto its geometric structure[28], and this has been a persistent obstacle in efforts to understand the mechanism of biological nitrogen fixation.

Our strategy for overcoming these challenges is to selectively enrich individual Fe sites of FeMo-co with ^{57}Fe (Fig. 1c). Analysis of such samples would simultaneously overcome issues of poor spectroscopic resolution and provide site-specific information on the chemical bonding at individual Fe centres. We recently reported[29] the initial development of this methodology using the L-cluster, an $[Fe_8S_9C]$ cluster that is a structural analogue of and biosynthetic precursor to FeMo-co (refs. [30,31]). In the present work, we adapted this ^{57}Fe-labelling procedure to FeMo-co and observed that the terminal site of FeMo-co (Fe1) can be selectively enriched with ^{57}Fe. Characterization of this sample enabled determination of the salient ^{57}Fe spectroscopic parameters for a particular Fe site in FeMo-co—the ^{57}Fe Mössbauer isomer shift (δ), the ^{57}Fe Mössbauer quadrupole splitting (ΔE_Q) and the ^{57}Fe electron–nuclear hyperfine coupling tensor ($A(^{57}Fe)$). Our findings reveal the Fe1 spin orientation and oxidation state in the M^N state, experimentally rule out a large number of potential FeMo-co electronic structures and test predictions made in previous computational studies. The oxidized resting state (M^{OX}) and the first intermediate in nitrogen fixation (E_1) were similarly analysed and the results are discussed here in the context of the redox chemistry of FeMo-co.

Results and discussion

Site-selective ^{57}Fe labelling of FeMo-co

Our approach to incorporating ^{57}Fe into the Fe1 site of FeMo-co entailed (1) using reported protocols[32] for extracting FeMo-co from the MoFe protein of the Mo nitrogenase (NifDK) into *N*-methylformamide (NMF), (2) removing the Fe1 site using a chelator, (3) reconstituting the Fe1 site with ^{57}Fe and (4) reinserting the labelled cofactor into apo-NifDK, which contains the P-cluster but not FeMo-co (see Methods for details). We first studied steps (2) and (3) by electron paramagnetic spectroscopy (EPR) spectroscopy (Fig. 2). When poised in the M^N state (obtained by incubation with sodium dithionite (DTH)), isolated FeMo-co exhibits a broadened $S = 3/2$ signal that sharpens in the presence of thiophenol (Fig. 2b, top)[33]. Previous work demonstrated that treating isolated FeMo-co with ethylenediaminetetraacetate (EDTA) or *o*-phenanthroline eliminates this signal, a process that can be reversed upon addition of Zn^{2+} or Fe^{2+}, respectively[34]; similarly, we found that adding excess $^{57}Fe^{2+}$ (35 equiv.) to EDTA-treated FeMo-co (30 equiv. EDTA) recovers the EPR signal (Fig. 2b, bottom), and, based on our findings with the L-cluster[29], we hypothesized that this protocol resulted in site-selective ^{57}Fe incorporation into the Fe1 site.

Encouraged by these results, we prepared NifDK samples with ^{57}Fe in either the Fe1 site or the six belt sites (Fe2–Fe7), as well as a control sample with ^{57}Fe in all seven sites (Fe1–Fe7; see Methods and Supplementary Information for details). The control sample was generated by isolating FeMo-co ($M(^{57}Fe_7)$) from fully ^{57}Fe-labelled NifDK, incubating the cofactor with the crude lysate from DJ1143 cells (an *Azotobacter vinelandii* strain that produces His-tagged apo-NifDK) and purifying the resulting holo-NifDK–$M(^{57}Fe_7)$. The Mössbauer spectrum of NifDK–$M(^{57}Fe_7)$ in the M^N state recorded at 80 K is consistent with previous reports[23,25,27,33] and shows a quadrupole doublet with an average isomer shift (δ_{avg}) of 0.39 mm s^{-1}, reflecting the overlapping signals from the seven Fe sites (vide infra).

https://doi.org/10.1038/s41557-023-01154-9

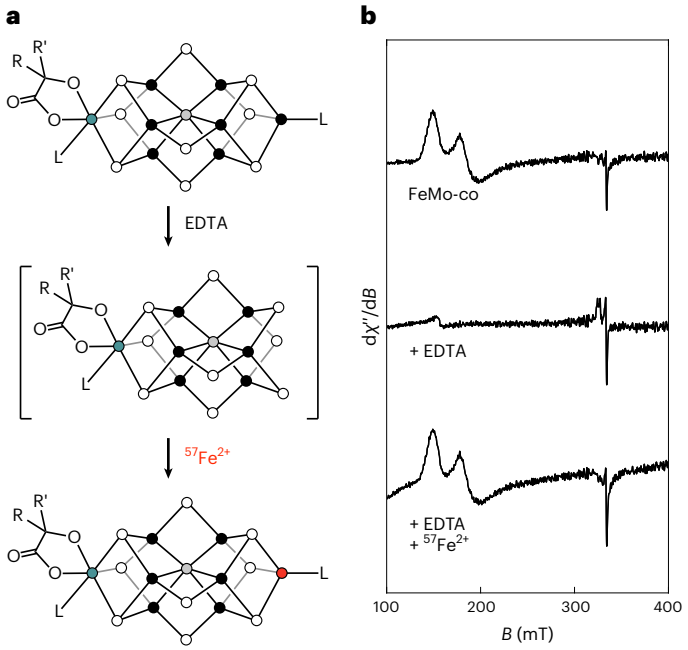

Fig. 2 | Postbiosynthetic incorporation of ^{57}Fe into FeMo-co. a, The chemical interconversions of isolated FeMo-co. **b**, The corresponding EPR spectra recorded at 9.37 GHz, 5 K and 1 mW. All EPR samples were incubated with DTH (2 mM) and PhSH (2 mM). χ'' is the imaginary part of the magnetic susceptibility; *B* is the applied magnetic field.

We subsequently generated the site-selectively labelled samples: NifDK–M($^{57}Fe_6$), by treating M($^{57}Fe_7$) with EDTA followed by natural abundance Fe^{2+}, and NifDK–M($^{57}Fe_1$), by treating natural abundance FeMo-co with EDTA followed by $^{57}Fe^{2+}$ (Fig. 3a). These samples, as well as NifDK–M($^{57}Fe_7$), showed full C_2H_2 reduction activity (Supplementary Table 20) and cleanly exhibited the $S = 3/2$ EPR signal of the native Mo nitrogenase resting state (Fig. 3b), demonstrating that our postbiosynthetic treatment with EDTA and Fe^{2+} did not affect FeMo-co's structure, composition or competency for reinsertion into apo-NifDK to generate active holo-NifDK. Analysis of the $^{56/57}$Fe content of the NifDK–M($^{57}Fe_1$) sample by inductively coupled plasma mass spectrometry (ICP-MS) indicated nearly quantitative labelling efficiency (~90% assuming complete site selectivity for the Fe1 site; see Supplementary Fig. 2 and Supplementary Information for further discussion). As discussed next, the essentially quantitative site selectivity of ^{57}Fe labelling is evident in both the Mössbauer and ENDOR spectra of these samples when poised in the M^N state (Fig. 3c,d).

ENDOR spectroscopic analysis of M^N

The Q-band ^{57}Fe ENDOR spectra of the three nitrogenase isotopologues in the M^N state recorded at g_3 are shown in Fig. 3c. The spectrum of NifDK–M($^{57}Fe_7$) (Fig. 3c, top) displays partially resolved signals that, as shown, are consistent with the predicted appearance of five [ν_-, ν_+] doublets, where $\nu_\pm = |\pm A/2 + \nu(^{57}Fe)|$, A is the hyperfine coupling determined from the previous analysis of the X-band ENDOR spectra and $\nu(^{57}Fe)$ is the ^{57}Fe Larmor frequency (3.4 MHz at 1,235 mT)[20,24]. (Note that although resting-state FeMo-co has $S = 3/2$, its EPR spectrum is discussed in terms of a 'fictitious spin', $S = 1/2$, with g values $\mathbf{g} = [g_1, g_2, g_3] = [4.32, 3.62, 2.01]$ (refs. [24,27]).) The corresponding spectrum of the NifDK–M($^{57}Fe_6$) sample, in which only the Fe2–Fe7 sites are enriched with ^{57}Fe (Fig. 3c, middle), retains four of those doublets and lacks the doublet denoted a^2 (observed in Fig. 3c, top), indicating that this doublet must arise from the Fe1 site. The assignment of this signal to Fe1 is confirmed by the spectrum of the NifDK–M($^{57}Fe_1$) sample, which shows only the a^2 doublet centred at the expected frequency, $A/2 = 9.8$ MHz. The complete elimination of the ν_+ peak of the a^2 doublet signal from the spectrum of NifDK–M($^{57}Fe_6$) (Fig. 3c, middle) indicates the high labelling efficiency for the Fe1 site, while the observation of only the a^2 doublet in the NifDK–M($^{57}Fe_1$) spectrum (Fig. 3c, bottom) and, in particular, the absence of any intensity from either peak of the sharp and intense a^1 doublet establish the high selectivity of our protocol.

In the original X-band study, the ^{57}Fe ENDOR spectra were well-resolved between $g_1 = 4.32$ and $g_2 = 3.62$ as well as at the high-field edge of the EPR spectrum at $g_3 = 2.01$, but poor resolution between g_2 and g_3 prevented direct experimental correlation between the responses from individual sites at the two 'ends' of the EPR spectrum. This 'gap' was addressed through ENDOR simulations, which indicated that the low-field A^2 signal evolved into the high-field a^2 doublet[24]. The present work confirms this correspondence between the A^2 and a^2 signals as well as the hyperfine tensor derived from the analysis of the field dependence of the X-band ENDOR signals. The Q-band ENDOR spectra of the selectively labelled NifDK–M($^{57}Fe_1$) sample recorded at $g_3 = 2.01$ and $g_1 = 4.30$ display features centred at ~10 and ~16 MHz, respectively (Fig. 4a), which are reproduced using the hyperfine tensor and associated Euler angles for a single ^{57}Fe site derived from the previous ENDOR simulations: hyperfine tensor principal components written in terms of the true $S = 3/2$ spin, $^T\mathbf{A} = [^TA_1, {}^TA_2, {}^TA_3] = [-14.0, -18.3, -19.5]$ MHz ($^TA_3$ increased by 3%), and the reported Euler angles, $\alpha = 10°$, $\beta = 15°$ and $\gamma = 0°$, defining the orientation of the hyperfine tensor frame relative to the g tensor frame (see Supplementary Information for further discussion)[24]. Notably, the finding that the observed Larmor splitting of the ^{57}Fe1 doublet at g_1 is 'nulled', such that a single peak is observed rather than a well-resolved doublet as seen at g_3 (Fig. 4a), directly reveals the Fe1 hyperfine coupling sign to be negative. The negative sign and the magnitude of the isotropic coupling for $^T\mathbf{A}$ of the Fe1 site, $^Ta_{iso} = -17.3$ MHz, together correspond to a vector-coupling coefficient for the spin of Fe1 of $K_1 \approx 0.87$, where $K_1 = 1$ implies that the Fe1 spin is exactly parallel to the cluster spin and $K_1 = 0$ implies that it is orthogonal[35]. Thus, the spin of Fe1 is essentially collinear with the overall electron spin of the cluster. This determination of the $A(^{57}Fe)$ hyperfine tensor corresponding to the Fe1 site, and thus the value of K_1, is critical for limiting the simulation space for magnetic Mössbauer experiments, delineating between the myriad broken-symmetry configurations for FeMo-co in the M^N state and interpreting other properties of FeMo-co, as discussed below.

Mössbauer spectroscopic analysis of M^N

The Mössbauer spectra of the three NifDK isotopologues (Fig. 3a) recorded at 80 K are shown in Fig. 3d (see Methods and Supplementary Information for details on Mössbauer data collection and analysis). As expected, the NifDK–M($^{57}Fe_7$) and NifDK–M($^{57}Fe_6$) spectra are very similar, each appearing as a single quadrupole doublet centred at $\delta_{avg} = 0.39$ and 0.38 mm s^{-1}, respectively, corresponding to the overlapping quadrupole doublets of all seven Fe sites and the six Fe belt sites, respectively. In contrast, the Mössbauer spectrum of NifDK–M($^{57}Fe_1$) features a quadrupole doublet centred at a considerably higher isomer shift of 0.49 mm s^{-1}. The spectra of NifDK–M($^{57}Fe_1$) and NifDK–M($^{57}Fe_7$) differ substantially, further demonstrating the site selectivity of the labelling protocol described above. The Mössbauer parameters at 80 K were obtained from simulations of the NifDK–M($^{57}Fe_7$), NifDK–M($^{57}Fe_6$) and NifDK–M($^{57}Fe_1$) spectra (Supplementary Tables 5 and 6; see Supplementary Information for details on the fitting procedure). Notably, the signal arising from the Fe1 site in NifDK–M($^{57}Fe_1$) is relatively broad, even at high temperatures, and its lineshape exhibits an unusual temperature dependence (Supplementary Fig. 3). As discussed in Supplementary Information, such behaviour could be ascribed to the thermal population and interconversion of low-lying excited states, although further analysis would be required to test this and alternative hypotheses.

https://doi.org/10.1038/s41557-023-01154-9

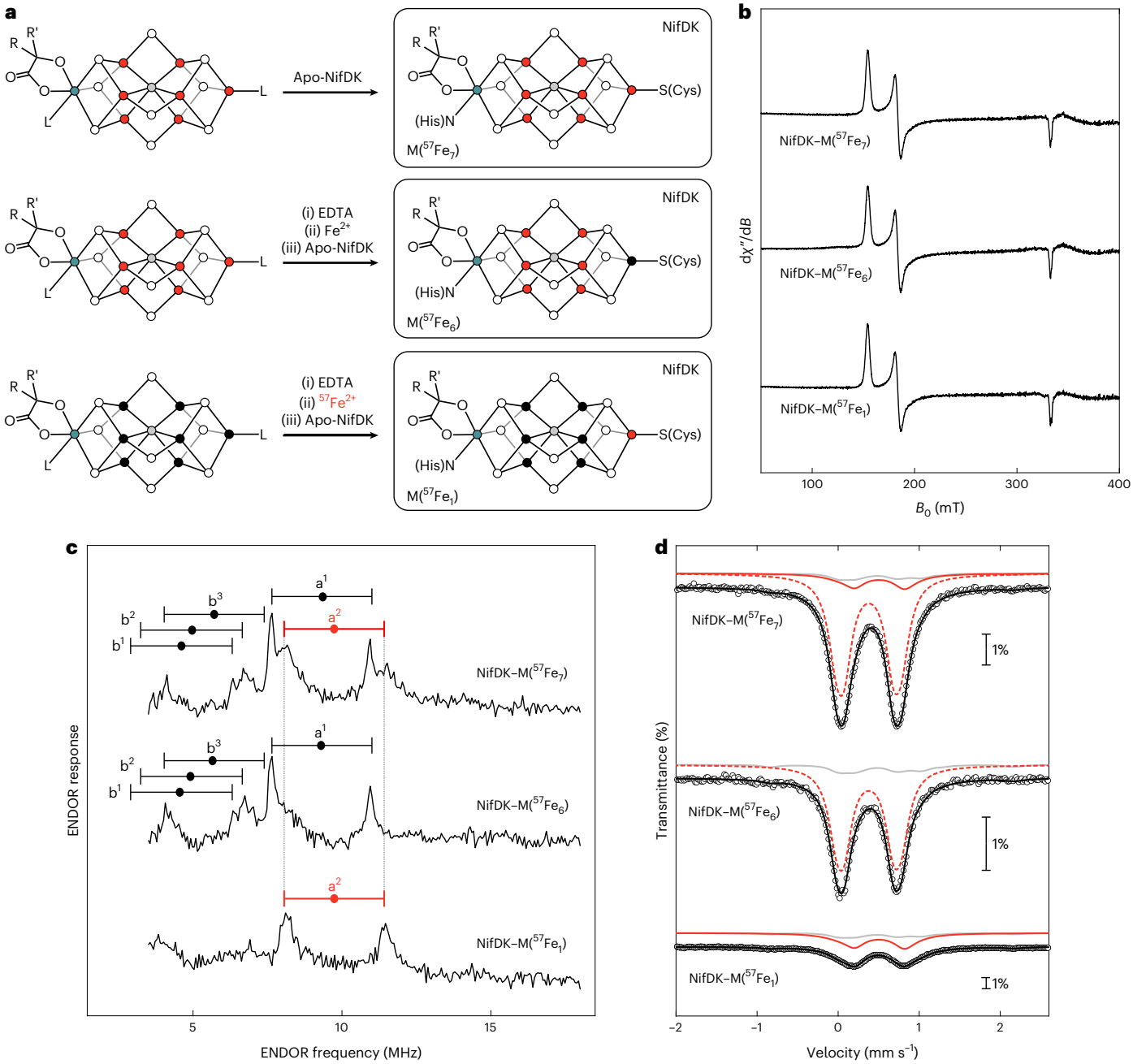

Fig. 3 | Preparation and characterization of site-selectively labelled holo-NifDK samples. a, Preparation of NifDK–M($^{57}Fe_7$), NifDK–M($^{57}Fe_6$) and NifDK–M($^{57}Fe_1$). **b**, EPR spectra of the samples recorded at 9.37 GHz, 5 K and 1 mW. **c**, ^{57}Fe Davies ENDOR spectra recorded at g_3 = 2.01 (1,235 mT), 34.745 GHz and 2 K, with pulse sequence parameters of $t(\pi/2)$ = 40 ns, τ = 600 ns, T_{RF} = 40 µs and repetition time = 15 ms. The positions of the [ν_-, ν_+] doublets are marked with 'goalposts'; label indicates the individual ^{57}Fe sites, as predicted from previously reported hyperfine tensors[25] (see text). **d**, Mössbauer spectra of the samples recorded at 80 K. Circles represent the experimental data; black traces show total simulations; solid red traces show simulations of the Fe1 site when labelled with ^{57}Fe; dashed red traces show simulations of the belt Fe sites when labelled with ^{57}Fe; grey traces show the spectrum of the NifDK–P($^{57}Fe_8$)–M($^{57}Fe_7$) sample (in which both the M-cluster and the P-cluster are enriched with ^{57}Fe), appropriately scaled to account for contributions from natural abundance ^{57}Fe. See Supplementary Information for details on data work-up and simulations. Note that a minor high-spin Fe^{2+} signal has been subtracted from the spectrum of NifDK–M($^{57}Fe_1$).

The ENDOR data provide $A(^{57}Fe)$ for the Fe1 site and unequivocally prove that the Fe1 site corresponds to the spectroscopic A^2 site; however, the Mössbauer hyperfine parameters for the A^2 site gleaned from low-temperature (4.2 K) studies of fully labelled samples[25] cannot be directly compared with our Mössbauer parameters determined at 80 K (vide supra). We therefore acquired and analysed Mössbauer spectra at low temperature (4.7 K) in the presence of a weak magnetic field (Fig. 4b). Using the $A(^{57}Fe1)$ hyperfine coupling tensor determined by ^{57}Fe ENDOR spectroscopy and taking into account the background signals from natural abundance ^{57}Fe (Fig. 4b, grey traces; see Supplementary Information for further discussion), we simulated the signal arising from the Fe1 site and thereby obtained the low-temperature Mössbauer hyperfine parameters: δ = 0.54 mm s^{-1} and the magnitude of ΔE_Q, $|\Delta E_Q|$ = 1.32 mm s^{-1} (Table 1). Notably, the values of δ and $|\Delta E_Q|$ for the Fe1 site obtained from the site-selectively labelled NifDK–M($^{57}Fe_1$) sample are higher than those proposed by Yoo et al. for any Fe site,

https://doi.org/10.1038/s41557-023-01154-9

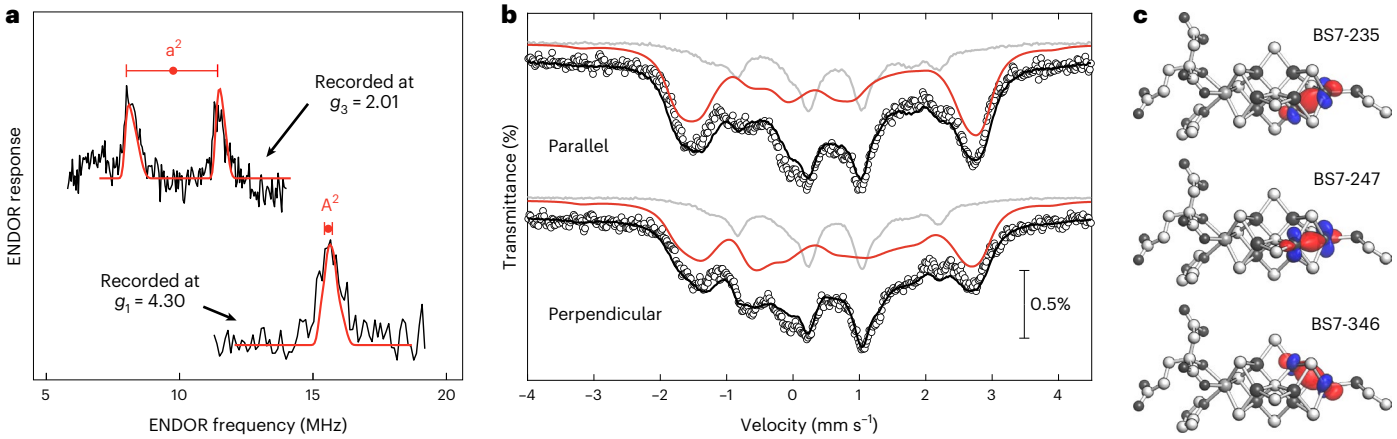

Fig. 4 | Characterization of the NifDK–M($^{57}Fe_1$) sample. a, ^{57}Fe Davies ENDOR spectra recorded at g_3 = 2.01 (1,235 mT; top) and g_1 = 4.30 (577 mT; bottom). The centre of each 'goalpost' equals the observed $A/2$ at that single-crystal-like g value; the breadth of each 'goalpost' equals twice the effective nuclear Larmor frequency. At g_1, the hyperfine coupling is strongly modified by the influence of the zero-field splitting of the true-spin S = 3/2 resting-state FeMo-co (Supplementary Information), while the observed Larmor splitting of the doublet at g_1 is essentially 'nulled', leaving a single peak, rather than exhibiting the doublet predicted for an isolated ^{57}Fe site (as seen at g_3, Fig. 3c). This nulling determines the sign of the ^{57}Fe1 hyperfine coupling, as it is a result of the combined effects of zero-field splitting and a large, negative hyperfine coupling, as discussed in the text. Simulations (red lines) were carried out as previously[25] using the parameters given in the text; the experimental parameters were the same as in Fig. 3. **b**, Mössbauer spectra recorded at 4.7 K in the presence of a 77 mT external field oriented parallel (top) or perpendicular (bottom) to the incident radiation. Circles represent the experimental data; black traces show the total simulations; red traces show the simulations for the Fe1 site (Table 1); grey traces show the spectra of the NifDK–P($^{57}Fe_8$)–M($^{57}Fe_7$) sample, appropriately scaled to account for contributions from natural abundance ^{57}Fe. Simulations performed using positive ΔE_Q are shown. See Supplementary Information for simulation details. **c**, Isosurface plots (0.05 a.u.) of the localized orbital qualitatively depicting the double-exchange interaction between the Fe1 site and the three indicated spin isomers. The plots were generated in the manner of Benediktsson and Bjornsson[14] (see Supplementary Information for details).

Table 1 | Low-temperature Mössbauer spectroscopic parameters for the Fe1 site in FeMo-co

Parameter	M^N (E_0)	M^{OX}	M^R (E_1)
δ (mm s^{-1})	0.54	0.36	0.53
$\lvert\Delta E_Q\rvert$ (mm s^{-1})	1.32	0.77	1.54
Γ (mm s^{-1})	0.39	0.26	0.36

See text and Supplementary Information for simulation details. M^R is the state of FeMo-co in E_1; Γ is the line width. The data for M^N and M^{OX} were recorded at 4.7 K; the data for M^R were recorded at 5.0 K.

including the A^2 site (0.48 and 0.94 mm s^{-1} at 4.2 K, respectively), based on simulations of NifDK–M($^{57}Fe_7$) (ref. [25]). This suggests that the Fe1 site has somewhat more electron density—and, correspondingly, that the six belt Fe sites have somewhat less—than indicated by previous Mössbauer analyses. The implications of this observation are discussed next.

Implications for the electronic structure of M^N

Fe–S clusters have been extensively characterized by Mössbauer spectroscopy[36], and thiolate-ligated [Fe_4S_4] clusters are particularly useful reference compounds for this study because they have an identical primary coordination sphere to that of the Fe1 site of FeMo-co: three μ_3-sulfides and one Cys thiolate. For [Fe_4S_4] clusters, FeMo-co and other high-nuclearity Fe–S clusters, the Fe oxidation states are typically assigned as Fe^{2+}, Fe^{3+} and/or $Fe^{2.5+}$, with $Fe^{2.5+}$ corresponding to an Fe in a mixed-valent Fe^{2+}–Fe^{3+} pair in which the excess electron is delocalized by the double-exchange mechanism[37,38]. Based on comparisons with [Fe_4S_4] clusters[36], the values of δ and $\lvert\Delta E_Q\rvert$ at 4.7 K for the Fe1 site are both too low for an Fe^{2+} site and too high for an Fe^{3+} site (see Supplementary Table 21). Indeed, they compare favourably with typical values for the $Fe^{2.5+}$ sites in [Fe_4S_4]$^+$ clusters (~0.5 and ~1.3 mm s^{-1}, respectively)[36]. Furthermore, using an empirical relationship[39] that relates the formal oxidation state and the Mössbauer isomer shifts of tetrahedral Fe sites in synthetic $FeS_n(SR)_{4-n}$ compounds, we arrive at an oxidation state of $Fe^{2.4+}$ for the Fe1 site in M^N. The assignment of an approximately $Fe^{2.5+}$ valence is further supported by comparison with the M^{OX} state (vide infra), and is broadly consistent with spatially resolved anomalous dispersion[28] and computational[13,14] analyses that indicate the Fe1 site is relatively reduced.

The identification of an $Fe^{2.5+}$ oxidation state for the Fe1 site necessitates that one of its neighbours, that is, Fe2, Fe3 or Fe4 (Figs. 1b and 4c), be the other member of the mixed-valent pair. This Fe site must be spin-aligned with Fe1 to undergo electron delocalization by the double-exchange mechanism, and it therefore must be one of the remaining A sites, which are each thought to have a $\delta \approx 0.4$ mm s^{-1} (ref. [25]). The relatively high δ for Fe1 indicates that, on the whole, the covalency of its Fe–ligand interactions (featuring bonds to three μ_3-sulfides and one Cys thiolate) is somewhat lower than that of its double-exchange-coupled partner (featuring bonds to two μ_3-sulfides, one μ_2-sulfide and one μ_6-carbide). This difference can be attributed at least in part to the greater Fe–S covalency of μ_2-sulfides compared with μ_3-sulfides and thiolates[40], and may also arise from covalent Fe–C bonding. Additionally, the difference in the coordination environments of the Fe sites could result in greater localization of the itinerate electron at the Fe1 site, and this effect would likewise contribute to a higher δ for Fe1.

The insights from spectroscopic analysis of the site-selectively labelled samples—in particular, that the spin of the Fe1 site is well-aligned with the overall electron spin of the cluster and that the Fe1 site is part of a mixed-valent pair of $Fe^{2.5+}$ centres—impose experimental constraints on the electronic structure of FeMo-co in the M^N state. All electronic configurations that invoke antiparallel spin alignment between the Fe1 site and the total spin can be rejected; this includes the BS3, BS6, BS9 and BS10 families of electronic structures (BS means broken symmetry) [10,41]. Our results also require that at least one of the neighbouring belt Fe sites (Fe2, Fe3 and Fe4) be co-aligned with Fe1 to engage in electron sharing by the double-exchange mechanism; this requirement further eliminates the BS2 family of electronic structures. Overall, these experimental findings are consistent with

https://doi.org/10.1038/s41557-023-01154-9

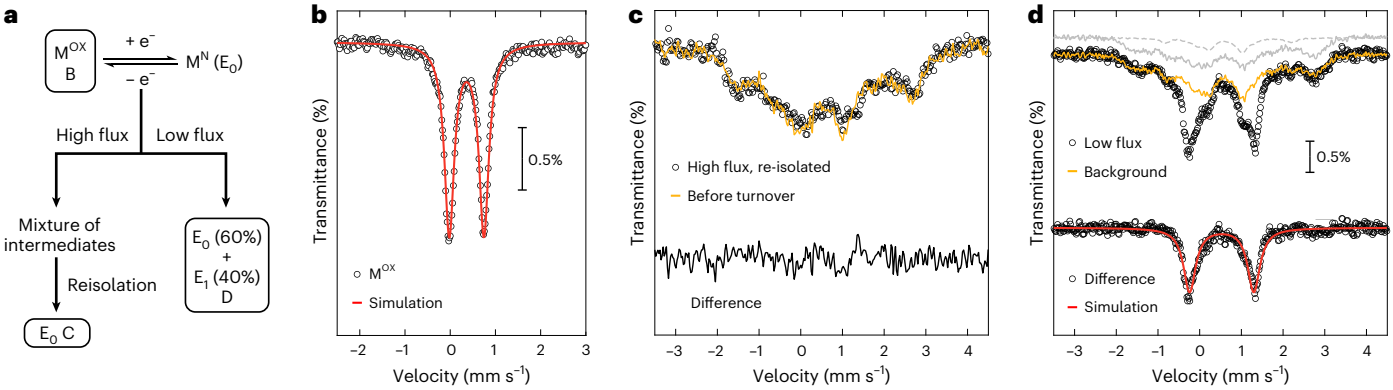

Fig. 5 | Redox changes at the Fe1 site of FeMo-co as revealed through studies of NifDK–M(^{57}Fe$_1$). **a**, Scheme showing how the M^{OX}, M^N (E$_0$) post-high-flux turnover and M^R (E$_1$) samples were generated. Labels B, C and D correspond to the panels in Fig. 5 in which the data are shown. **b**, Mössbauer spectrum and simulation of the sample poised in the M^{OX} state recorded at 4.7 K. Contributions from natural abundance ^{57}Fe have been subtracted (see Supplementary Information). **c**, Comparison of the Mössbauer spectra recorded at 5.0 K before and after high-flux turnover. The spectra were recorded in the presence of a 77 mT magnetic field (perpendicular) and normalized to the same integrated intensity. A difference spectrum is shown to highlight the similarity of the spectra. **d**, Mössbauer spectrum of the sample under low-flux turnover recorded at 5 K. Grey traces represent background signals from E$_1$ (in natural abundance; dashed) and E$_0$ (both enriched at Fe1 and in natural abundance; solid); the yellow trace is the sum of the grey traces. The difference between the low-flux spectrum and the background signals is shown at the bottom; the corresponding simulation reveals the Mössbauer parameters for the Fe1 site in M^R.

the electronic-structure picture favoured in recent computational analyses[13,14]: an [MoFe$_7$S$_9$C]$^-$ core charge state in the BS7 configuration, particularly the three spin isomers BS7-235, BS7-247 and BS7-346, which differ in the identity of the belt Fe that is aligned with the Fe1 site (Fig. 4c). In turn, the determination of the vector-coupling coefficient for ^{57}Fe1 plays an important role in assigning the function of the central FeMo-co carbon[42,43].

Characterization of M^{OX} and M^R

Having the ability to distinguish between the valences of the Fe1 and belt Fe sites, we next characterized other states of FeMo-co to determine whether redox changes occur at the Fe1 site, the belt Fe sites or both. We began with M^{OX} because comparison of its individual metal valences with those of M^N would reveal the site(s) of M^N that are most reducing. The reversible oxidation of M^N to M^{OX} has been reported previously[44], and we adapted this procedure to poise the NifDK–M(^{57}Fe$_7$), NifDK–M(^{57}Fe$_6$) and NifDK–M(^{57}Fe$_1$) samples in the M^{OX} state (Fig. 5a, Methods and Supplementary Fig. 6). The ground spin state of M^{OX} is $S = 0$ (refs. [44,45]), and its Mössbauer spectra do not exhibit magnetic splitting even at low temperature (Fig. 5b and Supplementary Fig. 6)[44,46–48]. Comparison of the Mössbauer parameters for the Fe1 site in the M^N and M^{OX} states at 4.7 K (Table 1) reveals a striking shift in hyperfine parameters: δ decreases from 0.54 to 0.36 mm s^{-1} upon oxidation, and $|\Delta E_Q|$ likewise decreases from 1.32 to 0.77 mm s^{-1}. Although substantial, the magnitude of the decrease in δ (0.18 mm s^{-1}) is smaller than what would be expected for a localized Fe^{2+} to Fe^{3+} redox event (~0.4 mm s^{-1}) and is instead consistent with the conversion of an $Fe^{2.5+}$ site to an Fe^{3+} site (Supplementary Table 22)[36]. The value of δ_{avg} for the belt sites at 80 K decreases modestly upon oxidation from 0.38 mm s^{-1} in M^N to 0.33 mm s^{-1} in M^{OX}. The magnitude of this change (~0.05 mm s^{-1} over six sites, or 0.30 mm s^{-1} in total) is likewise consistent with the removal of approximately half an electron from the six belt sites (compare with the Mössbauer spectra of $[Fe_4S_4]^{2+/+}$ clusters, whose isomer shifts differ by ~0.48 mm s^{-1} per electron when normalized to one site). We therefore conclude that the Fe1 site and its double-exchange-coupled partner are redox active in the interconversion of M^N and M^{OX}, and it follows that these metal centres are the most electron rich in M^N.

Using our site-selectively labelled samples to characterize intermediates in N$_2$ reduction catalysis requires that the ^{57}Fe label at the Fe1 site is not lost and does not scramble into other sites during turnover (the latter possibility is raised by evidence for turnover-mediated Fe–S bond cleavage in FeMo-co)[49–52]. To test whether site-selective labelling is maintained during catalysis, we subjected the NifDK–M(^{57}Fe$_1$) sample to high-flux turnover conditions under N$_2$ for 30 min (Methods), re-isolated NifDK from the reaction mixture and reanalysed its metal content and spectroscopic properties. The ^{57}Fe/^{56}Fe ratio determined by ICP-MS analysis was the same pre- and post-turnover (Supplementary Information), and the low-temperature Mössbauer spectrum (Fig. 5c) of the post-turnover sample features the same characteristic pattern of the Fe1 site as found in the pre-turnover sample, particularly at the high- and low-energy edges of the spectrum (around 2.8 and −1.7 mm s^{-1}). The foregoing results demonstrate that little to no loss or scrambling of the ^{57}Fe1 label occurs during turnover and that intermediates generated using NifDK–M(^{57}Fe$_1$) samples will retain their ^{57}Fe label with high site selectivity.

Finally, we exploited these findings to characterize the first intermediate in N$_2$ reduction, E$_1$, which is generated upon the addition of a proton and an electron to E$_0$. Because the E$_1$ state of FeMo-co is not EPR active, it cannot be characterized by ^{57}Fe ENDOR spectroscopy; instead, previous characterization of E$_1$ has relied on techniques (Mössbauer and X-ray absorption spectroscopy) that, owing to their poor resolution, do not permit resolution of the individual Fe sites[23,25,53,54]. Moreover, no experiments have elucidated the properties of a crystallographically defined Fe site in E$_1$ or in any other intermediate. We therefore sought to apply site-selective labelling to overcome these challenges.

Following reported protocols[23,25,53,54], we subjected the NifDK–M(^{57}Fe$_1$) sample to low-flux turnover conditions, generating a mixture of E$_0$ and E$_1$ in a ratio of ~60:40 (see Methods and Supplementary Information for details), each with FeMo-co in a reduced state (M^N and M^R for E$_0$ and E$_1$, respectively). The resulting Mössbauer spectrum recorded at 5.0 K (Fig. 5d) contains contributions from the signal of interest—the enriched Fe1 site in the E$_1$ state—as well as background signals from (1) the enriched Fe1 site in the E$_0$ (M^N) state, (2) the Fe2–Fe6 centres in both states at natural abundance and (3) the P-cluster (in the P^N state in both E$_0$ and E$_1$) at natural abundance. Subtracting these background signals (see Supplementary Information for details) leaves a clean quadrupole doublet (Fig. 5d) corresponding to the Fe1 site in E$_1$ with the following parameters: $\delta = 0.53$ mm s^{-1} and $|\Delta E_Q| = 1.54$ mm s^{-1}. The similarity in the Mössbauer hyperfine parameters for the Fe1 site in E$_0$ and E$_1$ therefore reveals that the proton and electron loaded into FeMo-co in the transition from E$_0$ to E$_1$ are localized at sites other than

Fe1, either in a metal–hydride bond (in the case of metal-based protonation, as has been suggested by analogy to the all-Fe nitrogenase)[55] or in a metal-based orbital (in the case of S-based protonation, as has been suggested by spectroscopic and computational studies)[53,56]; the Fe1 site remains part of a spin-aligned pair of $Fe^{2.5+}$ sites with an unchanged primary coordination sphere.

Conclusion

We have reported here a chemical method for the site-selective incorporation of ^{57}Fe into FeMo-co and showed how analysis of site-selectively labelled samples informs on the distribution and coupling of valence electrons in FeMo-co. The ^{57}Fe ENDOR analysis of M^N links the crystallographic Fe1 site to the spectroscopic A^2 site, and thereby experimentally connects the electronic properties of an individual site with the geometric structure of FeMo-co. We have further shown that (1) the Fe1 site is part of a mixed-valent pair of $Fe^{2.5+}$ ions, (2) that this pair is the most reduced moiety in the resting state, and (3) that the valence and primary coordination sphere is maintained for the Fe1 site in E_1, the first intermediate of N_2 reduction. Overall, these findings place experimental constraints on the electronic structure of FeMo-co in multiple states, while the observation that the ^{57}Fe label in the Fe1 site does not scramble during turnover demonstrates the promise of site-selective isotope editing for providing insights into the mechanism of biological nitrogen fixation.

Online content

Any methods, additional references, Nature Portfolio reporting summaries, source data, extended data, supplementary information, acknowledgements, peer review information; details of author contributions and competing interests; and statements of data and code availability are available at https://doi.org/10.1038/s41557-023-01154-9.

References

1. Raymond, J., Siefert, J. L., Staples, C. R. & Blankenship, R. E. The natural history of nitrogen fixation. *Mol. Biol. Evol.* **21**, 541–554 (2004).
2. Canfield, D. E., Glazer, A. N. & Falkowski, P. G. The evolution and future of Earth's nitrogen cycle. *Science* **330**, 192–196 (2010).
3. Hoffman, B. M., Lukoyanov, D., Yang, Z.-Y., Dean, D. R. & Seefeldt, L. C. Mechanism of nitrogen fixation by nitrogenase: the next stage. *Chem. Rev.* **114**, 4041–4062 (2014).
4. Winter, H. C. & Burris, R. H. Nitrogenase. *Annu. Rev. Biochem.* **45**, 409–426 (1976).
5. Burgess, B. K. & Lowe, D. J. Mechanism of molybdenum nitrogenase. *Chem. Rev.* **96**, 2983–3012 (1996).
6. Van Stappen, C. et al. The spectroscopy of nitrogenases. *Chem. Rev.* **120**, 5005–5081 (2020).
7. Einsle, O. & Rees, D. C. Structural enzymology of nitrogenase enzymes. *Chem. Rev.* **120**, 4969–5004 (2020).
8. Seefeldt, L. C. et al. Reduction of substrates by nitrogenases. *Chem. Rev.* **120**, 5082–5106 (2020).
9. Spatzal, T. et al. Evidence for interstitial carbon in nitrogenase FeMo cofactor. *Science* **334**, 940 (2011).
10. Lovell, T., Li, J., Liu, T., Case, D. A. & Noodleman, L. FeMo cofactor of nitrogenase: a density functional study of states M^N, M^{OX}, M^R, and M^I. *J. Am. Chem. Soc.* **123**, 12392–12410 (2001).
11. Harris, T. V. & Szilagyi, R. K. Comparative assessment of the composition and charge state of nitrogenase FeMo-cofactor. *Inorg. Chem.* **50**, 4811–4824 (2011).
12. Siegbahn, P. E. M. Model calculations suggest that the central carbon in the FeMo-cofactor of nitrogenase becomes protonated in the process of nitrogen fixation. *J. Am. Chem. Soc.* **138**, 10485–10495 (2016).
13. Bjornsson, R., Neese, F. & DeBeer, S. Revisiting the Mössbauer isomer shifts of the FeMoco cluster of nitrogenase and the cofactor charge. *Inorg. Chem.* **56**, 1470–1477 (2017).
14. Benediktsson, B. & Bjornsson, R. QM/MM study of the nitrogenase MoFe protein resting state: broken-symmetry states, protonation states, and QM region convergence in the FeMoco active site. *Inorg. Chem.* **56**, 13417–13429 (2017).
15. Raugei, S., Seefeldt, L. C. & Hoffman, B. M. Critical computational analysis illuminates the reductive-elimination mechanism that activates nitrogenase for N_2 reduction. *Proc. Natl Acad. Sci. USA* **115**, E10521 (2018).
16. Li, Z., Li, J., Dattani, N. S., Umrigar, C. J. & Chan, G. K.-L. The electronic complexity of the ground-state of the FeMo cofactor of nitrogenase as relevant to quantum simulations. *J. Chem. Phys.* **150**, 024302 (2019).
17. Cramer, S. P., Hodgson, K. O., Gillum, W. O. & Mortenson, L. E. The molybdenum site of nitrogenase. Preliminary structural evidence from X-ray absorption spectroscopy. *J. Am. Chem. Soc.* **100**, 3398–3407 (1978).
18. Cramer, S. P. et al. The molybdenum site of nitrogenase. 2. A comparative study of molybdenum–iron proteins and the iron–molybdenum cofactor by X-ray absorption spectroscopy. *J. Am. Chem. Soc.* **100**, 3814–3819 (1978).
19. Conradson, S. D. et al. Structural insights from the molybdenum K-edge X-ray absorption near edge structure of the iron–molybdenum protein of nitrogenase and its iron–molybdenum cofactor by comparison with synthetic iron–molybdenum–sulfur clusters. *J. Am. Chem. Soc.* **107**, 7935–7940 (1985).
20. Venters, R. A. et al. ENDOR of the resting state of nitrogenase molybdenum–iron proteins from *Azotobacter vinelandii*, *Klebsiella pneumoniae*, and *Clostridium pasteurianum*. Proton, iron-57, molybdenum-95, and sulfur-33 studies. *J. Am. Chem. Soc.* **108**, 3487–3498 (1986).
21. Lukoyanov, D., Yang, Z.-Y., Dean, D. R., Seefeldt, L. C. & Hoffman, B. M. Is Mo involved in hydride binding by the four-electron reduced (E_4) intermediate of the nitrogenase MoFe protein? *J. Am. Chem. Soc.* **132**, 2526–2527 (2010).
22. Bjornsson, R. et al. Identification of a spin-coupled Mo(III) in the nitrogenase iron–molybdenum cofactor. *Chem. Sci.* **5**, 3096–3103 (2014).
23. Van Stappen, C. et al. Spectroscopic description of the E_1 state of Mo nitrogenase based on Mo and Fe X-ray absorption and Mössbauer studies. *Inorg. Chem.* **58**, 12365–12376 (2019).
24. True, A. E., Nelson, M. J., Venters, R. A., Orme-Johnson, W. H. & Hoffman, B. M. Iron-57 hyperfine coupling tensors of the FeMo cluster in *Azotobacter vinelandii* MoFe protein: determination by polycrystalline ENDOR spectroscopy. *J. Am. Chem. Soc.* **110**, 1935–1943 (1988).
25. Yoo, S. J., Angove, H. C., Papaefthymiou, V., Burgess, B. K. & Münck, E. Mössbauer study of the MoFe protein of nitrogenase from *Azotobacter vinelandii* using selective ^{57}Fe enrichment of the M-centers. *J. Am. Chem. Soc.* **122**, 4926–4936 (2000).
26. Lukoyanov, D. A. et al. Electron redistribution within the nitrogenase active site FeMo-cofactor during reductive elimination of H_2 to achieve N≡N triple-bond activation. *J. Am. Chem. Soc.* **142**, 21679–21690 (2020).
27. Münck, E. et al. Nitrogenase. VIII. Mössbauer and EPR spectroscopy. The MoFe protein component from *Azotobacter vinelandii* OP. *Biochim. Biophys. Acta Protein Struct.* **400**, 32–53 (1975).
28. Spatzal, T. et al. Nitrogenase FeMoco investigated by spatially resolved anomalous dispersion refinement. *Nat. Commun.* **7**, 10902 (2016).
29. Srisantitham, S., Badding, E. D. & Suess, D. L. M. Postbiosynthetic modification of a precursor to the nitrogenase iron–molybdenum cofactor. *Proc. Natl Acad. Sci. USA* **118**, e2015361118 (2021).
30. Ribbe, M. W., Hu, Y., Hodgson, K. O. & Hedman, B. Biosynthesis of nitrogenase metalloclusters. *Chem. Rev.* **114**, 4063–4080 (2014).

31. Burén, S., Jiménez-Vicente, E., Echavarri-Erasun, C. & Rubio, L. M. Biosynthesis of nitrogenase cofactors. *Chem. Rev.* **120**, 4921–4968 (2020).
32. Shah, V. K. & Brill, W. J. Isolation of an iron–molybdenum cofactor from nitrogenase. *Proc. Natl Acad. Sci. USA* **74**, 3249–3253 (1977).
33. Rawlings, J. et al. Novel metal cluster in the iron–molybdenum cofactor of nitrogenase. Spectroscopic evidence. *J. Biol. Chem.* **253**, 1001–1004 (1978).
34. Yang, S. S. et al. Iron–molybdenum cofactor from nitrogenase. Modified extraction methods as probes for composition. *J. Biol. Chem.* **257**, 8042–8048 (1982).
35. Mouesca, J. M., Noodleman, L., Case, D. A. & Lamotte, B. Spin densities and spin coupling in iron–sulfur clusters: a new analysis of hyperfine coupling constants. *Inorg. Chem.* **34**, 4347–4359 (1995).
36. Pandelia, M.-E., Lanz, N. D., Booker, S. J. & Krebs, C. Mössbauer spectroscopy of Fe/S proteins. *Biochim. Biophys. Acta Mol. Cell Res.* **1853**, 1395–1405 (2015).
37. Papaefthymiou, V., Girerd, J. J., Moura, I., Moura, J. J. G. & Muenck, E. Moessbauer study of *D. gigas* ferredoxin II and spin-coupling model for Fe_3S_4 cluster with valence delocalization. *J. Am. Chem. Soc.* **109**, 4703–4710 (1987).
38. Noodleman, L. Exchange coupling and resonance delocalization in reduced iron–sulfur $[Fe_4S_4]^+$ and iron–selenium $[Fe_4Se_4]^+$ clusters. 1. Basic theory of spin-state energies and EPR and hyperfine properties. *Inorg. Chem.* **30**, 246–256 (1991).
39. Venkateswara Rao, P. & Holm, R. H. Synthetic analogues of the active sites of iron–sulfur proteins. *Chem. Rev.* **104**, 527–560 (2004).
40. Solomon, E. I., Gorelsky, S. I. & Dey, A. Metal–thiolate bonds in bioinorganic chemistry. *J. Comput. Chem.* **27**, 1415–1428 (2006).
41. Lukoyanov, D. et al. Testing if the interstitial atom, X, of the nitrogenase molybdenum–iron cofactor is N or C: ENDOR, ESEEM, and DFT studies of the $S = 3/2$ resting state in multiple environments. *Inorg. Chem.* **46**, 11437–11449 (2007).
42. Lukoyanov, D. A. et al. ^{13}C ENDOR characterization of the central carbon within the nitrogenase catalytic cofactor indicates that the CFe_6 core is a stabilizing 'heart of steel'. *J. Am. Chem. Soc.* **144**, 18315–18328 (2022).
43. Pérez-González, A. et al. Exploring the role of the central carbide of the nitrogenase active-site FeMo-cofactor through targeted ^{13}C labeling and ENDOR spectroscopy. *J. Am. Chem. Soc.* **143**, 9183–9190 (2021).
44. Zimmermann, R. et al. Nitrogenase X: Mössbauer and EPR studies on reversibly oxidized MoFe protein from *Azotobacter vinelandii* OP. Nature of the iron centers. *Biochim. Biophys. Acta Protein Struct.* **537**, 185–207 (1978).
45. Johnson, M. K., Thomson, A. J., Robinson, A. E. & Smith, B. E. Characterization of the paramagnetic centres of the molybdenum–iron protein of nitrogenase from *Klebsiella pneumoniae* using low temperature magnetic circular dichroism spectroscopy. *Biochim. Biophys. Acta Protein Struct.* **671**, 61–70 (1981).
46. Lindahl, P. A., Papaefthymiou, V., Orme-Johnson, W. H. & Münck, E. Mössbauer studies of solid thionin-oxidized MoFe protein of nitrogenase. *J. Biol. Chem.* **263**, 19412–19418 (1988).
47. Smith, B. E. & Lang, G. Mössbauer spectroscopy of the nitrogenase proteins from *Klebsiella pneumoniae*. Structural assignments and mechanistic conclusions. *Biochem. J* **137**, 169–180 (1974).
48. Surerus, K. K. et al. Moessbauer and integer-spin EPR of the oxidized P-clusters of nitrogenase: P^{OX} is a non-Kramers system with a nearly degenerate ground doublet. *J. Am. Chem. Soc.* **114**, 8579–8590 (1992).
49. Spatzal, T., Perez, K. A., Einsle, O., Howard, J. B. & Rees, D. C. Ligand binding to the FeMo-cofactor: structures of CO-bound and reactivated nitrogenase. *Science* **345**, 1620–1623 (2014).
50. Spatzal, T., Perez, K. A., Howard, J. B. & Rees, D. C. Catalysis-dependent selenium incorporation and migration in the nitrogenase active site iron–molybdenum cofactor. *eLife* **4**, e11620 (2015).
51. Kang, W., Lee, C. C., Jasniewski, A. J., Ribbe, M. W. & Hu, Y. Structural evidence for a dynamic metallocofactor during N_2 reduction by Mo-nitrogenase. *Science* **368**, 1381–1385 (2020).
52. Lee, C. C. et al. Evidence of substrate binding and product release via belt-sulfur mobilization of the nitrogenase cofactor. *Nat. Catal.* **5**, 443–454 (2022).
53. Van Stappen, C., Thorhallsson, A. T., Decamps, L., Bjornsson, R. & DeBeer, S. Resolving the structure of the E_1 state of Mo nitrogenase through Mo and Fe K-edge EXAFS and QM/MM calculations. *Chem. Sci.* **10**, 9807–9821 (2019).
54. Christiansen, J., Tittsworth, R. C., Hales, B. J. & Cramer, S. P. Fe and Mo EXAFS of *Azotobacter vinelandii* nitrogenase in partially oxidized and singly reduced forms. *J. Am. Chem. Soc.* **117**, 10017–10024 (1995).
55. Lukoyanov, D. A. et al. The one-electron reduced active-site FeFe-cofactor of Fe-nitrogenase contains a hydride bound to a formally oxidized metal-ion core. *Inorg. Chem.* **61**, 5459–5464 (2022).
56. Cao, L., Caldararu, O. & Ryde, U. Protonation and reduction of the FeMo cluster in nitrogenase studied by quantum mechanics/molecular mechanics (QM/MM) calculations. *J. Comput. Chem.* **14**, 6653–6678 (2018).

Methods

Cell growth

The *Azotobacter vinelandii* strains employed in this study (wild-type (WT), DJ1141, producing His-tagged NifDK, and DJ1143, producing His-tagged apo-NifDK) were cultured in 18-l batches in a 20-l B. Braun Biostat C bioreactor using Burk's minimal medium. For the growth of WT and DJ1141, cultures were supplemented with 6 mM ammonium acetate, derepression was initiated upon ammonium depletion, cells were collected after 3 h by centrifugation at 7,000*g* for 4 min, and the cell paste was flash-frozen in liquid N_2 (LN_2) and stored at −80 °C until purification[57]. For the growth of the DJ1143 strain, cultures were supplemented with 10 mM urea, cells were grown to an optical density at 600 nm of 4.0, the cells were pelleted by centrifugation at 7,000*g* for 4 min, derepression was initiated by resuspending the pelleted cells in Burk's minimum medium containing no urea for 3 h, the cells were again collected by centrifugation at 7,000*g* for 4 min, and the cell paste was flash-frozen in LN_2 and stored at −80 °C until needed. Finally, ^{57}Fe-enriched NifDK protein was generated by the above protocols using ^{57}Fe (generated by dissolving ^{57}Fe powder (Trace Science International, 95.5% enrichment) in stoichiometric H_2SO_4).

NifDK purification

NifDK was purified in a Coy Labs glove box (<5 ppm O_2). All solutions were sparged with N_2 overnight. Cells were lysed using the osmotic shock method as follows: DJ1141 cell paste was resuspended in 3 ml of 25 mM HEPES (pH 7.5), 50% glycerol and 2 mM DTH for every gram of cell paste. After stirring at room temperature for 15 min, the cells were pelleted at 25,000*g* for 15 min. The supernatant was poured off and the pelleted cells were resuspended in 3 ml buffer containing 25 mM HEPES (pH 7.5), 2 mM DTH, 3 mM phenylmethylsulfonyl fluoride, 1 mg ml^{-1} lysozyme and 100 µg ml^{-1} DNase I for every gram of cell paste. After stirring for 15 min, the lysate was pelleted at 100,000*g* for 1 h and loaded onto a Co-nitriloacetic acid (NTA) column equilibrated with buffer containing 500 mM NaCl, 25 mM HEPES (pH 7.5), 20% glycerol and 2 mM DTH. The immobilized protein was washed with ten column volumes of equilibration buffer and eluted with equilibration buffer containing 200 mM imidazole. NifDK was further purified using anion exchange chromatography: the protein solution was diluted fourfold with buffer containing 25 mM HEPES (pH 7.5), 20% glycerol and 2 mM DTH and then loaded onto a diethylaminoethyl-sepharose column charged with NaCl and equilibrated with the dilution buffer. The column was washed with ten column volumes of 160 mM NaCl, 25 mM HEPES (pH 7.5), 2 mM DTH and 20% glycerol. The immobilized protein was then eluted with buffer containing 500 mM NaCl, 25 mM HEPES (pH 7.5), 2 mM DTH and 20% glycerol. Purified NifDK was concentrated using an AMICON stirred cell equipped with a 30 kDa filter and then flash-frozen and stored in LN_2. The concentration of NifDK was estimated by determining the Mo content using ICP-MS. Note that in our study, the reported concentrations of NifDK are based on the αβ heterodimer concentration (with one FeMo-co per heterodimer in holo-NifDK) rather than the $\alpha_2\beta_2$ heterotetramer concentration (with two FeMo-co per heterotetramer in holo-NifDK).

NifH purification

NifH was purified in an MBRAUN glove box (<5 ppm O_2) following a procedure similar to that previously reported[58]. WT *A. vinelandii* cell paste was lysed as described above. Lysate was loaded onto a DE-52 column charged with NaCl and equilibrated in 25 mM HEPES (pH 7.5) and 2 mM DTH. The column was washed with a buffer with a stepwise gradient of 125, 200, 300 and 500 mM NaCl. Fractions were analysed by EPR spectroscopy; those determined to contain NifH were pooled and concentrated using a DE-52 cellulose column and AMICON spin filters equipped with a 10 kDa filter. NifH was then purified further using a Superdex 200 column equilibrated with buffer containing 200 mM NaCl, 25 mM HEPES (pH 7.5) and 2 mM DTH. Purified NifH was subsequently concentrated and flash-frozen in LN_2. The concentration of NifH was estimated by UV–visible spectroscopy[58].

FeMo-co isolation

The protocol for FeMo-co isolation was adapted from a previously reported procedure[32]. Protein manipulation was performed in a Coy Labs glove box (<5 ppm O_2) and FeMo-co manipulation was carried out in an MBRAUN or Vacuum Atmospheres glove box (<5 ppm O_2). NifDK (typical protein concentrations ranging from 100 to 400 µM αβ dimer) was diluted tenfold with aqueous 2 mM DTH. The protein was denatured by the addition of 100 mM citric acid (1.67 ml per 10 ml of diluted protein) added dropwise at 0 °C with stirring. After incubating the mixture for 30 s, the protein was precipitated by the addition of 200 mM Na_2HPO_4 (1.7 ml per 10 ml of diluted protein). The precipitated protein was transferred to a 15-ml conical tube and moved to the MBRAUN glove box where the protein was pelleted at 120*g* for 5 min using a Labnet Z100A centrifuge. The supernatant was removed and the pellet was washed with *N,N*-dimethylformamide (5 ml) and pelleted. This washing step with *N,N*-dimethylformamide was performed once more. FeMo-co was then extracted by resuspending and vortexing the pellet with 1–2 ml NMF containing 2 mM Na_2HPO_4 (from a 200 mM aqueous stock solution). After incubation for 5 min at room temperature, the extract was centrifuged at 500*g* for 5 min and the brown supernatant was collected. This process was repeated until the solution was colourless, and the extracts were then combined. The concentration of FeMo-co was estimated by UV–visible spectroscopy using an extinction coefficient of PhS-bound FeMo-co in NMF of 14,800 M^{-1} cm^{-1} at 450 nm (Supplementary Fig. 19).

Acetylene reduction activity assays

The specific activity of NifDK was assessed using the acetylene reduction activity assay. Assays were performed in 10-ml crimped vials under an atmosphere of 90:10 argon/acetylene in a water bath at 30 °C. Each assay contained 800 µl ATP mix (25 mM Tris buffer (pH 7.9), 30 mM creatine phosphate disodium salt, 5 mM ATP disodium salt, 5 mM $MgCl_2$, 25 units ml^{-1} phosphocreatine kinase and 20 mM DTH), 100 µg NifDK and 435 µg NifH. Assays were initiated with the addition of NifH and quenched after 6 min with 100 µl of 4 M NaOH. Ethylene production was measured by injecting 50 µl of headspace into an Agilent 6890N gas chromatograph equipped with a flame ionization detector and an HP-PLOT/Q 30 m × 0.319 mm × 20.00 µm column. Ethylene standards were prepared by injecting 1 ml ethylene into gravimetrically calibrated round-bottomed flasks containing 1 atm air.

Postbiosynthetic isotope editing of FeMo-co

Isolated FeMo-co (either ^{57}Fe-enriched or natural abundance) was treated with 30 equiv. EDTA (added as a 100 mM aqueous stock solution) and stirred at room temperature for 5 min. Then 35 equiv. $FeCl_2$ (either natural abundance or ^{57}Fe-enriched) was added (as a 100 mM stock solution in 50% (v/v) NMF–H_2O) and the solution was stirred for 3 min at room temperature. Prolonged incubation of EDTA-treated FeMo-co with $FeCl_2$ can lead to the appearance of an unidentified $S = 5/2$ EPR signal ($g_{eff} = 4.3$); however, samples with this signal are competent for FeMo-co insertion into apo-NifDK, and as such the reaction with excess $FeCl_2$ appears to be reversible.

Insertion of FeMoco into apo-NifDK

The procedure for inserting FeMo-co into apo-NifDK protein was adapted from previous reports[59,60]. Excess as-isolated or

postbiosynthetically modified FeMo-co (up to 1.5 equiv.) was added dropwise to freshly prepared crude lysate of DJ1143 (lysed using the osmotic shock method) with stirring at room temperature. The final concentration of NMF was approximately 1% (v/v). Once FeMo-co addition was complete, the now holo-NifDK protein was purified as described above with an additional step. Following anion exchange chromatography, the NifDK protein was applied to a Superdex 200 column equilibrated in 500 mM NaCl, 25 mM HEPES (pH 7.5), 20% glycerol and 2 mM DTH. Fractions containing NifDK were pooled and concentrated. Note that we estimated that 1 g of DJ1143 cell paste grown by the method described above contains ~10 nmol apo-NifDK; this value was determined by measuring the isolated yield of apo-NifDK across several purifications from a fixed amount of DJ1143 cell paste.

ENDOR sample preparation

The NifDK–M($^{57}Fe_7$), NifDK–M($^{57}Fe_6$) and NifDK–M($^{57}Fe_1$) samples were prepared as discussed above with an additional step. Some samples contained small amounts of Co impurities that were likely introduced in the Co-NTA purification step. Although this is not an issue for acquiring Mössbauer data, these impurities can be observed in the EPR spectra. To remove these Co impurities for ENDOR analysis, the holo-NifDK samples were incubated with EDTA several times using the following procedure. Samples (~350 µl in volume and containing ~100–300 µM Mo) were incubated with EDTA-containing buffer (~10 equiv. EDTA per Mo, 500 mM NaCl, 25 mM HEPES (pH 7.5), 20% glycerol and 2 mM DTH) by repeated cycles of concentration and dilution using an AMICON centrifugal spin filter (30 kDa cut-off). Approximately every five to seven cycles, samples were assessed by EPR analysis to determine whether the Co had been removed. EDTA was then removed by the same concentration and dilution protocol, but with buffer that did not contain EDTA. This protocol did not affect the intensity or shape of the $S = 3/2$ signal of FeMo-co, although it did lower the specific activity of C_2H_2 reduction to approximately 60% of the pretreatment activity (Supplementary Table 20). The final concentration of all ^{57}Fe ENDOR samples was ~100 µM.

Mössbauer sample preparation

Samples were poised in the M^N state by incubation with DTH. Samples were poised in the M^{OX} state by (1) treatment with 500 µM indigo disulfonate, (2) gel filtration into buffer containing 500 mM NaCl, 25 mM HEPES (pH 7.5) and 20% glycerol using a PD-10 column (GE Healthcare), and (3) incubation with 7 equiv. phenazine methosulfate (stoichiometry based on Mo concentration) for 3 min before freezing in LN_2.

Samples containing the turnover state E_1 were generated by adding NifH (in a ratio of 100:1 NifDK/NifH) to NifDK in PD-10 equilibration buffer (see above) containing 5 mM ATP, 5 mM $MgCl_2$, 20 mM phosphocreatine, 30 mM sodium dithionite and 25 U ml^{-1} creatine kinase. The sample was freeze-quenched in LN_2 after approximately 5 min. The yield of E_1 was determined by the loss of the resting-state EPR signal of NifDK as determined by continuous-wave EPR spectroscopy (Supplementary Figs. 12 and 13).

The post-turnover (high-flux) sample was prepared by diluting the NifDK–M($^{57}Fe_1$) Mössbauer sample to 20 µM with storage buffer that contained 5 mM $MgCl_2$, 5 mM ATP, 20 mM phosphocreatine, 30 mM DTH and 25 U ml^{-1} creatine kinase. Turnover was initiated by the addition of NifH to a final concentration of 20 µM; this ratio of components corresponds to high-flux turnover conditions[61]. After 30 min, the sample was purified using an Ni-NTA column and gel-filtered into storage buffer before being flash-frozen in LN_2.

Spectroscopy and spectrometry

Zero-field ^{57}Fe Mössbauer spectra were recorded with a SEE W302 constant-acceleration spectrometer equipped with a JANIS closed-cycle He gas refrigerator cryostat (5–200 K). Isomer shifts are quoted relative to α-Fe foil at room temperature. EPR samples were prepared in an anaerobic glove box under N_2 atmosphere with an O_2 level of <5 ppm. X-band EPR spectra were recorded on a Bruker EMX spectrometer at 9.37 GHz. Q-band ENDOR data were collected using a lab-built spectrometer[62].

ICP-MS data were acquired with an Agilent 7900 ICP-MS instrument. Protein samples were digested with concentrated nitric acid (TraceMetal grade, Fischer) at 70 °C and diluted with Milli-Q water to a final concentration of 2% nitric acid. Standards for Mo were prepared from a 1,000 ppm standard solution (VWR BDH Chemicals). Standards for Fe and ^{56}Fe were prepared from a 1,000 ppm standard solution (SPEX Certiprep). Standards for ^{57}Fe were prepared as described previously[29]. The concentrations of ^{56}Fe and ^{57}Fe in the standard solutions were based on the natural abundance of each isotope in the unenriched standard (91.7% ^{56}Fe and 2.12% ^{57}Fe) and the isotope enrichment in ^{57}Fe powder (95.5% ^{57}Fe and 3.6% ^{56}Fe).

Reporting summary

Further information on research design is available in the Nature Portfolio Reporting Summary linked to this article.

Data availability

Data supporting the findings of this work are available within the article and its Supplementary Information. Data supporting the current study are also available from the corresponding author upon request. PDB 3U7Q was used in the preparation of Fig. 1.

References

57. Lee, C.-C., Ribbe, M. W. & Hu, Y. in *Metalloproteins: Methods and Protocols* (ed. Hu, Y.) 111–124 (Springer, 2019).
58. Burgess, B. K., Jacobs, D. B. & Stiefel, E. I. Large-scale purification of high activity *Azotobacter vinelandII* nitrogenase. *Biochim. Biophys. Acta Enzymol.* **614**, 196–209 (1980).
59. McLean, P. A., Papaefthymiou, V., Orme-Johnson, W. H. & Münck, E. Isotopic hybrids of nitrogenase. Mössbauer study of MoFe protein with selective ^{57}Fe enrichment of the P-cluster. *J. Biol. Chem.* **262**, 12900–12903 (1987).
60. Christiansen, J., Goodwin, P. J., Lanzilotta, W. N., Seefeldt, L. C. & Dean, D. R. Catalytic and biophysical properties of a nitrogenase apo-MoFe protein produced by a *nifB*-deletion mutant of *Azotobacter vinelandii*. *Biochemistry* **37**, 12611–12623 (1998).
61. Harris, D. F., Yang, Z.-Y., Dean, D. R., Seefeldt, L. C. & Hoffman, B. M. Kinetic understanding of N_2 reduction versus H_2 evolution at the E_4(4H) Janus state in the three nitrogenases. *Biochemistry* **57**, 5706–5714 (2018).
62. Davoust, C. E., Doan, P. E. & Hoffman, B. M. Q-band pulsed electron spin-echo spectrometer and its application to ENDOR and ESEEM. *J. Magn. Reson. A* **119**, 38–44 (1996).

Acknowledgements

We acknowledge the National Institutes of Health (GM141203 to D.L.M.S. and GM111097 to B.M.H.), the MIT Research Support Committee (to D.L.M.S.) and the National Science Foundation (MCB-1908587 to B.M.H.) for funding. We thank N. Thompson for helpful discussions as well as D. Dean and V. Cash for providing the *Azotobacter vinelandii* strains used in this work. Support for the ICP-MS instrument was provided by a core centre grant (P30-ES002109) from the National Institute of Environmental Health Sciences, NIH.

Author contributions

E.D.B., S.S. and D.A.L. performed the experiments. All authors contributed to the design of the study, data analysis and paper writing.

Competing interests

The authors declare no competing interests.

Additional information

Supplementary information The online version contains supplementary material available at https://doi.org/10.1038/s41557-023-01154-9.

Correspondence and requests for materials should be addressed to Daniel L. M. Suess.

Peer review information *Nature Chemistry* thanks Lou Noodleman and the other, anonymous, reviewer(s) for their contribution to the peer review of this work.

nature portfolio

Corresponding author(s): Daniel L. M. Suess

Last updated by author(s): Nov 29, 2022

Reporting Summary

Nature Portfolio wishes to improve the reproducibility of the work that we publish. This form provides structure for consistency and transparency in reporting. For further information on Nature Portfolio policies, see our Editorial Policies and the Editorial Policy Checklist.

Statistics

For all statistical analyses, confirm that the following items are present in the figure legend, table legend, main text, or Methods section.

n/a	Confirmed	
☒	☐	The exact sample size (*n*) for each experimental group/condition, given as a discrete number and unit of measurement
☒	☐	A statement on whether measurements were taken from distinct samples or whether the same sample was measured repeatedly
☒	☐	The statistical test(s) used AND whether they are one- or two-sided *Only common tests should be described solely by name; describe more complex techniques in the Methods section.*
☒	☐	A description of all covariates tested
☒	☐	A description of any assumptions or corrections, such as tests of normality and adjustment for multiple comparisons
☒	☐	A full description of the statistical parameters including central tendency (e.g. means) or other basic estimates (e.g. regression coefficient) AND variation (e.g. standard deviation) or associated estimates of uncertainty (e.g. confidence intervals)
☒	☐	For null hypothesis testing, the test statistic (e.g. *F*, *t*, *r*) with confidence intervals, effect sizes, degrees of freedom and *P* value noted *Give P values as exact values whenever suitable.*
☒	☐	For Bayesian analysis, information on the choice of priors and Markov chain Monte Carlo settings
☒	☐	For hierarchical and complex designs, identification of the appropriate level for tests and full reporting of outcomes
☒	☐	Estimates of effect sizes (e.g. Cohen's *d*, Pearson's *r*), indicating how they were calculated

Our web collection on statistics for biologists contains articles on many of the points above.

Software and code

Policy information about availability of computer code

Data collection	Mössbauer data collection: W302 from SEE Co; EPR data collection: Xenon v1.1b.155 from Bruker, and Spectrometer Manager v1.1; ICP data collection: Masshunter Workstation v4.1 from Agilent; UV-vis data collection: Scan v3.0 from Cary Instruments
Data analysis	Mössbauer data analysis: WMOSS4 vF and Matlab R2021b; EPR and UV-vis data analysis: Matlab R2021b; computational analysis: ORCA v4.1.2 and Visual Molecular Dynamics v1.9.4

For manuscripts utilizing custom algorithms or software that are central to the research but not yet described in published literature, software must be made available to editors and reviewers. We strongly encourage code deposition in a community repository (e.g. GitHub). See the Nature Portfolio guidelines for submitting code & software for further information.

Data

Policy information about availability of data

All manuscripts must include a data availability statement. This statement should provide the following information, where applicable:

- Accession codes, unique identifiers, or web links for publicly available datasets
- A description of any restrictions on data availability
- For clinical datasets or third party data, please ensure that the statement adheres to our policy

There are no appropriate repositories for the datasets generated during and/or analysed during the current study. As such, the datasets are available from the corresponding author on reasonable request. PDB 3U7Q was used in the preparation of Fig. 1.

Human research participants

Policy information about studies involving human research participants and Sex and Gender in Research.

Reporting on sex and gender	N/A
Population characteristics	N/A
Recruitment	N/A
Ethics oversight	N/A

Note that full information on the approval of the study protocol must also be provided in the manuscript.

Field-specific reporting

Please select the one below that is the best fit for your research. If you are not sure, read the appropriate sections before making your selection.

☒ Life sciences ☐ Behavioural & social sciences ☐ Ecological, evolutionary & environmental sciences

For a reference copy of the document with all sections, see nature.com/documents/nr-reporting-summary-flat.pdf

Life sciences study design

All studies must disclose on these points even when the disclosure is negative.

Sample size	This is not relevant because the life sciences component of this research entailed only following previously reported protocols for bacterial growth and protein overexpression (see: Lee, C.-C., Ribbe, M. W. & Hu, Y., Purification of Nitrogenase Proteins. In Metalloproteins: 600 Methods and Protocols, Hu, Y., Ed. Springer New York: New York, NY, 2019; pp 111-124). As such, "sample size" is not a relevant consideration.
Data exclusions	No data were excluded from the analyses.
Replication	The site-selectively labeled samples have been generated and characterized at least twice, and all attempts at replication were successful.
Randomization	This is not relevant because "experimental groups" are not well-defined in our study.
Blinding	This is not relevant because "experimental groups" are not well-defined in our study.

Reporting for specific materials, systems and methods

We require information from authors about some types of materials, experimental systems and methods used in many studies. Here, indicate whether each material, system or method listed is relevant to your study. If you are not sure if a list item applies to your research, read the appropriate section before selecting a response.

Materials & experimental systems

n/a	Involved in the study
☒	☐ Antibodies
☒	☐ Eukaryotic cell lines
☒	☐ Palaeontology and archaeology
☒	☐ Animals and other organisms
☒	☐ Clinical data
☒	☐ Dual use research of concern

Methods

n/a	Involved in the study
☒	☐ ChIP-seq
☒	☐ Flow cytometry
☒	☐ MRI-based neuroimaging